

Normal and Abnormal Pathology Knowledge-Augmented Vision-Language Model for Anomaly Detection in Pathology Images

Jinsol Song¹ Jiamu Wang¹ Anh Tien Nguyen¹ Keunho Byeon¹
 Sangjeong Ahn¹ Sung Hak Lee² Jin Tae Kwak¹
¹Korea University ²The Catholic University of Korea

Jinsol Song: truetcg@korea.ac.kr Jin Tae Kwak: jkwak@korea.ac.kr

Abstract

Anomaly detection in computational pathology aims to identify rare and scarce anomalies where disease-related data are often limited or missing. Existing anomaly detection methods, primarily designed for industrial settings, face limitations in pathology due to computational constraints, diverse tissue structures, and lack of interpretability. To address these challenges, we propose Ano-NAViLa, a Normal and Abnormal pathology knowledge-augmented Vision-Language model for Anomaly detection in pathology images. Ano-NAViLa is built on a pre-trained vision-language model with a lightweight trainable MLP. By incorporating both normal and abnormal pathology knowledge, Ano-NAViLa enhances accuracy and robustness to variability in pathology images and provides interpretability through image-text associations. Evaluated on two lymph node datasets from different organs, Ano-NAViLa achieves the state-of-the-art performance in anomaly detection and localization, outperforming competing models.

1. Introduction

Anomaly detection (AD) has been a long-standing research area dedicated to addressing the practical challenge of detecting anomalies, which are inherently scarce and difficult to collect compared to normal data. While AD can be considered as a binary classification task, it differs from standard classification as it exclusively learns from normal data to identify deviations indicative of anomalies. Most existing research has focused on developing visual AD models for applications such as quality inspection and defect detection in industrial settings [4, 31, 34]. In computational pathology, specific disease conditions are often rare but hold critical clinical implications [9, 50], posing a significant challenge. Therefore, AD holds great potential to improve clinical practice by enabling the identification of rare disease patterns with limited labeled data.

There are several limitations when applying existing methods to pathology images: 1) *Computational bottleneck*: State-of-the-art AD models often rely on large backbone networks [8, 13, 45], requiring substantial memory storage [7, 32], or adopt generative models [21, 42] with long inference times, making them impractical for real-world applications. Gigapixel-sized whole slide images (WSIs) [19] impose even greater computational and storage demands; 2) *Tissue Diversity*: Anomalies, e.g., scratches, damages, and missing components, in other domains, are often well-defined, whereas, in pathology images, anomalies are more complex and diverse, involving intricate alterations in cellular and tissue structures. Even normal tissues exhibit high structural heterogeneity [50], making it more challenging to differentiate between normal variations and true anomalies; 3) *Generalization ability*: The quality of pathology images considerably varies due to multiple factors, including differences in institutions, imaging equipment, and staining protocols. These variations contribute to domain shifts, limiting the generalizability of existing AD methods across different domains; 4) *Interpretability*: Most existing AD methods operate as black-boxes, providing minimal insight into their final decisions. This lack of interpretability restricts their adoption in real-world clinical settings, where transparency is crucial to support trustworthiness and clinically relevant decision-making.

To address these challenges, we propose Ano-NAViLa, a Normal and Abnormal pathology knowledge-augmented Vision-Language model for Anomaly detection in pathology images. Ano-NAViLa is built by integrating a vision-language model (VLM) for feature extraction and semantic mapping with multi-layer perceptrons (MLPs) for anomaly clustering and detection. The model is designed to utilize two types of pathology knowledge to enhance its AD capabilities: 1) *Data-driven knowledge*: Ano-NAViLa adopts a pathology VLM, pre-trained on large pathology image-text pair datasets, to obtain rich image and text representations, which are subsequently used to extract distinctive features between normal and abnormal tissues; 2) *Ex-*

pert (Pathologist-guided) knowledge: Ano-NAViLa incorporates structured and curated pathology terms provided by experts, ensuring that the model learns clinically relevant patterns and improves interpretability in detecting and analyzing abnormal tissue structures. Notably, Ano-NAViLa utilizes both normal and abnormal pathology terms that illustrate the normal structure of tissues as well as structural and morphological alterations due to disease progression.

The key advantages of Ano-NAViLa are three-folds: 1) *Computational efficiency:* Ano-NAViLa is designed as a lightweight architecture. The pre-trained VLM remains frozen, while only the MLP is optimized during training, substantially reducing computational overhead and supporting faster training and inference. 2) *Robustness to variability in data:* Ano-NAViLa uses both normal and abnormal pathology terms, describing structural variations and alterations within each category and across the two categories. This approach is universally applicable to all pathology datasets, minimizing data-specific biases. 3) *Transparency to pathologists:* Leveraging the image-text alignment, Ano-NAViLa provides textual description for both normal and abnormal images. This allows pathologists to understand, validate, and interpret the predictions, making the AD process becomes interpretable and clinically meaningful.

To evaluate Ano-NAViLa, we employ two independent datasets for lymph node metastasis detection: 1) GastricLN: A private gastric dataset used to train, validate, and test Ano-NAViLa; 2) Camelyon16 [10]: A public breast dataset used as an external test set to assess the model’s generalization ability. The experimental results demonstrate that Ano-NAViLa achieves superior AD performance, surpassing existing state-of-the-art AD models. More importantly, Ano-NAViLa permits clear visualization of most metastatic regions, with improved interpretability through histologically meaningful text descriptions. In contrast, competing models struggle to distinctly localize metastases and lack interpretability. These findings highlight the effectiveness of Ano-NAViLa as an accurate, robust, and interpretable AD solution for pathology images.

2. Related Work

Visual anomaly detection. Earlier AD methods primarily adopted classical techniques like support vector machine (SVM) [6] and principal component analysis (PCA) [40]. Recent advances in deep learning has improved AD performance, with approaches divided into two major categories: 1) Reconstruction-based methods, such as autoencoder [3, 41], variational autoencoder [22, 37], generative adversarial networks (GANs) [1, 25, 36], and diffusion models [21, 42, 43], are designed to reconstruct normal data only and utilize reconstruction errors as an indicator for AD. Among them, diffusion models have achieved promising results but are limited by high computational cost and

risk of reconstructing out-of-distribution images too well, reducing their effectiveness in AD. 2) Representation-based methods aim to learn feature representations for enhanced estimation and modeling of normal data distributions. A prominent approach is memory bank-based methods that store image features and apply various techniques, such as k-Nearest Neighbor (kNN) algorithm [27, 32] and Mahalanobis distance [7, 30]. However, these methods face scalability issues due to their large storage requirements. Other approaches include Gaussian distribution modeling [29, 51] for density estimation, employing normalizing flows [13, 33, 45] to estimate the likelihood of normality, and hypersphere-based feature learning [20, 23, 44].

Another AD approach adopts the student–teacher framework, based on the assumption that the output difference between the two networks will be larger for anomalous data. Typically, the two networks share identical architecture [2, 5, 38], allowing for a simple distillation process and low latency, while some explored hybrid architectures [34, 35]. VLM-based approaches have also emerged for AD. WinCLIP [16] aggregates image features with similarities to collected normal and abnormal text prompts, while AnomalyCLIP [48] optimizes text prompts to enhance class separation. InCTRL [49] extracts image features guided by text prompts and detects anomalies based on residuals from few-shot normal samples. These methods leverage pre-trained models for strong few/zero-shot performance, but make limited use of the interpretability offered by VLMs.

Pathology vision-language models. VLMs serve as a foundation for numerous vision-language tasks. Notable examples include CLIP [28] and ALIGN [17], which employ contrastive learning to train a dual encoder for aligning images and texts. SimVLM [39] adopts generative image-to-text learning with an encoder-decoder structure. CoCa [46] combines both contrastive and generative learning for improved multimodal image-text representations. Driven by these advancements, several VLMs have been introduced for pathology image analysis. For instance, PLIP [14] is trained on a 208K pathology images paired with natural language descriptions, BiomedCLIP [47] is trained on multimodal medical dataset covering microscopy, biosignals, scientific diagrams, and flowcharts, QuiltNet [15] is trained on 1M pathology image-text pairs, and CONCH [24] is based on CoCa and trained on a dataset with 1.17 million image-caption pairs.

3. Method

Ano-NAViLa consists of four key components: 1) normal and abnormal term pools; 2) a VLM with visual and text encoders; 3) a trainable MLP; 4) an anomaly scoring scheme. Using a pre-trained VLM \mathcal{V} , an input image x is processed by its visual encoder, producing an image embedding. Simultaneously, the text encoder of \mathcal{V} converts terms from the

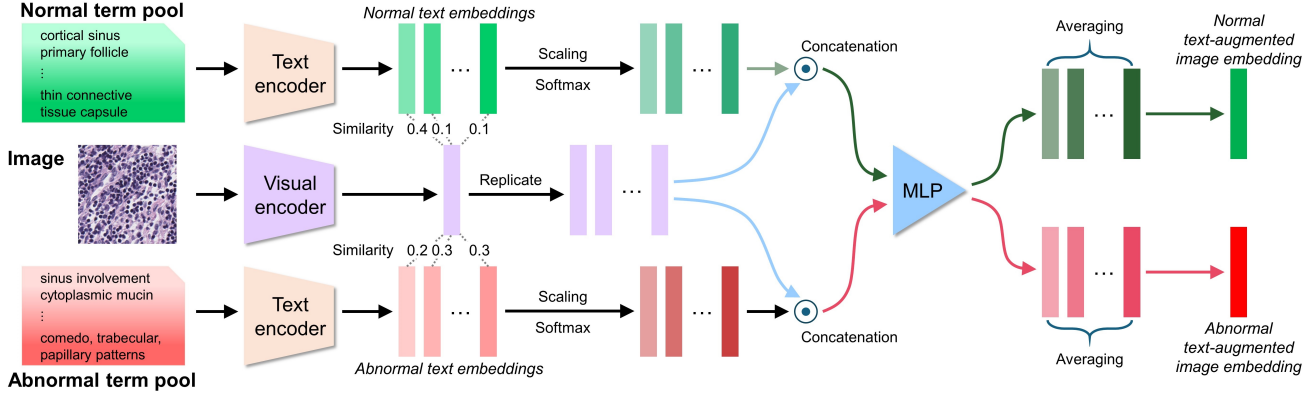


Figure 1. Generation of normal and abnormal text-augmented image embeddings. Two embeddings are generated for each image, representing its relationship with the normal and abnormal term pools, respectively. Only the MLP is trainable throughout the entire process.

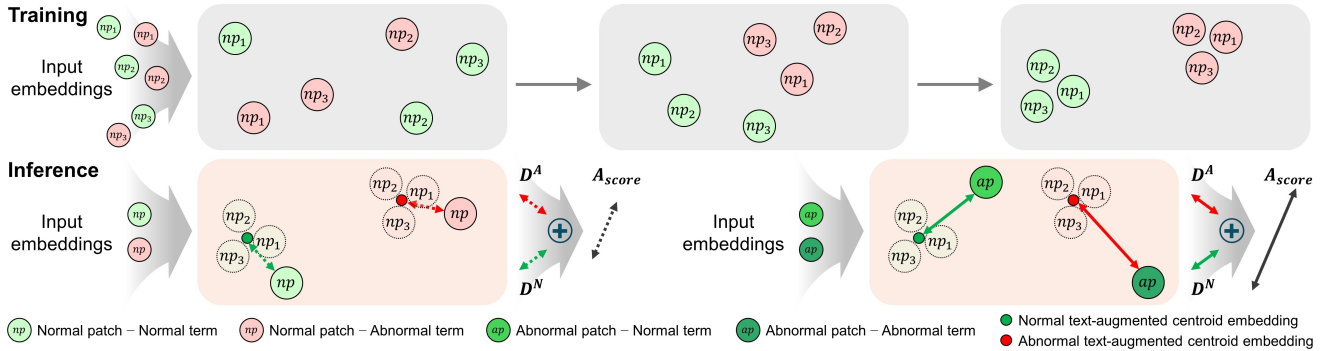


Figure 2. Training and inference procedures. The MLP is trained using only normal images to separately cluster embeddings that are representative of normal image–normal term and normal image–abnormal term relations. At inference, the distances from the two cluster centroids are computed, and their sum serves as the anomaly score, with larger values indicative of anomalies.

two term pools into text embeddings. Through image-text alignment, these text embeddings are normalized and concatenated with the image embedding. Finally, the MLP produces text-augmented image embeddings, which are used to compute anomaly scores, effectively distinguish normal images from abnormal images.

3.1. Construction of term pools

We collect a set of pathology terms related to the target pathology images. Focusing on AD, these terms are categorized into two distinct pools, forming a normal term pool $T^N = \{t_i^N\}_{i=1}^{n_N}$ and an abnormal term pool $T^A = \{t_j^A\}_{j=1}^{n_A}$ where t_i^N and t_j^A represent the i th normal term and the j th abnormal term, respectively, and n_N and n_A denote the total number of terms in the normal and abnormal term pools, respectively. The key idea is that images interact differently with the normal and abnormal terms. By training a model to recognize these distinctions, we aim to emulate human experts’ decision-making process, identifying anomalous images through their associations and contrasts with both normal and abnormal pathology terms. For lymph node

metastasis detection, relevant pathology terms are collected from literature, mostly based on [12], thoroughly selected and validated by an experienced pathologist. The curated term pools consist of 92 normal and 48 abnormal pathology terms, which are available in the supplementary material.

3.2. Text-augmented image representations

Ano-NAViLa is inspired by TQx [26], which yields the representation of an image as a weighted sum of the top- k text embeddings from a pathology term pool. We generate VLM-based feature representations for pathology images by concatenating the image embedding with each text embedding, which are then processed by a MLP to produce dynamic representations. We use two distinct pathology term pools—normal and abnormal—to learn their specific associations with each image for AD. Fig. 1 illustrates the procedure of generating VLM-based feature representations.

Suppose that we are given a normal pathology image x . Let Γ be a VLM and ρ be a MLP. Γ has an visual encoder Γ^V and a text encoder Γ^T . For x , we generate an image embedding $\mathbf{v}^I = \Gamma^V(x) \in \mathbb{R}^{512}$. Provided with T^N

and T^A , we produce their corresponding text embeddings $\mathbf{v}^N = \{\Gamma^T(t_i^N)\}_{i=1}^{n_N}$ and $\mathbf{v}^A = \{\Gamma^T(t_j^A)\}_{j=1}^{n_A}$, both in \mathbb{R}^{512} , respectively. Each text embedding is associated with the image embedding \mathbf{v}^I using cosine similarity (c_{sim}). The similarity scores are then normalized through the Softmax function and serve as weights for the text embeddings:

$$w_i^N = \frac{\exp[c_{sim}(\mathbf{v}^I, \mathbf{v}_i^N)]}{\sum_k \exp[c_{sim}(\mathbf{v}^I, \mathbf{v}_k^N)]}, w_j^A = \frac{\exp[c_{sim}(\mathbf{v}^I, \mathbf{v}_j^A)]}{\sum_k \exp[c_{sim}(\mathbf{v}^I, \mathbf{v}_k^A)]} \quad (1)$$

where w_i^N and w_j^A are the corresponding weights for \mathbf{v}_i^N and \mathbf{v}_j^A , respectively. These weights, which typically fall within the range $[0, 0.1]$, are scale up using an exponential function. After weighing the text embeddings, each text embedding is concatenated with the image embedding \mathbf{v}^I , forming a vector in \mathbb{R}^{1024} , which is then passed through the MLP ρ , yielding two image-text embeddings as follows:

$$\mathbf{u}_i^N = \rho(\mathbf{v}^I \circ (e^{w_i^N} \cdot \mathbf{v}_i^N)), \mathbf{u}_j^A = \rho(\mathbf{v}^I \circ (e^{w_j^A} \cdot \mathbf{v}_j^A)) \quad (2)$$

where \mathbf{u}_i^N and \mathbf{u}_j^A denote the i th image-normal and j th image-abnormal text embeddings, respectively, and \circ is the concatenation operation. Finally, by averaging all image-text embeddings in each category, we obtain the representative normal text-augmented image embedding \mathbf{h}^N and abnormal text-augmented image embedding \mathbf{h}^A for the given image x . In this manner, pathology terms with higher similarity with the image x contribute more to the final representations. Consequently, the final representation reflects the relationship between the image and the corresponding text pool. We note that we employ CONCH [24] as Γ , which is frozen throughout the entire procedure, and the MLP ρ is the only trainable component.

3.3. Optimization: Contrastive learning

The goal of the MLP ρ is to obtain text-augmented image embeddings in a latent space where embeddings within the same category (i.e., driven by normal pathology terms or abnormal pathology terms) are closely clustered, while two categories are pushed further apart to enhance separability. To achieve this, we propose the following loss function:

$$\mathcal{L} = -\log \left[\frac{S_{\text{intra}}(\mathbf{h}^N) + S_{\text{intra}}(\mathbf{h}^A)}{S_{\text{intra}}(\mathbf{h}^N) + S_{\text{intra}}(\mathbf{h}^A) + S_{\text{inter}}(\mathbf{h}^N, \mathbf{h}^A)} \right], \quad (3)$$

$$S_{\text{intra}}(\mathbf{h}^N) = \frac{1}{Z_1} \sum_{i=1}^{B-1} \sum_{j=i+1}^B \exp[c_{sim}(\mathbf{h}_i^N, \mathbf{h}_j^N)], \quad (4)$$

$$S_{\text{intra}}(\mathbf{h}^A) = \frac{1}{Z_1} \sum_{i=1}^{B-1} \sum_{j=i+1}^B \exp[c_{sim}(\mathbf{h}_i^A, \mathbf{h}_j^A)], \quad (5)$$

$$S_{\text{inter}}(\mathbf{h}^N, \mathbf{h}^A) = \frac{1}{Z_2} \sum_{i=1}^B \sum_{j=1}^B \exp[c_{sim}(\mathbf{h}_i^N, \mathbf{h}_j^A)] \quad (6)$$

where B is the batch size, \mathbf{h}_i^N and \mathbf{h}_i^A denote the normal and abnormal text-augmented image embeddings for the i th image x_i , respectively, and $Z_1 = \binom{B}{2}$ and $Z_2 = B^2$ are

normalization factors. By minimizing \mathcal{L} , we aim to maximize intra-group similarity S_{intra} for each pool category, while minimizing inter-group similarity S_{inter} between the two pool categories. Fig. 2 illustrates the training process. Though the MLP ρ is trained exclusively on normal images without involving abnormal images during optimization, the interaction between normal images with abnormal pathology terms function as a regularization mechanism, further enhancing representation power of normal images.

3.4. Anomaly score and inference

By training the MLP, the model learns two distinct relationships: normal images to normal terms, and normal images to abnormal terms. The two resulting clusters, representing these relationships, are located separately in the feature space. Therefore, an abnormal image is expected to align differently with both normal and abnormal terms compared to normal images, which allows us to compute an anomaly score based on its relative position to the two clusters.

To facilitate AD at the patch-level, we first compute two centroid text-augmented image embeddings from normal images, denoted as $\bar{\mathbf{h}}^N$ and $\bar{\mathbf{h}}^A$, for the normal and abnormal pathology term pools, respectively. These two centroid embeddings are used to calculate the deviations from the normal distribution. Specifically, given an input image x , we produce the corresponding embeddings \mathbf{h}^N and \mathbf{h}^A , and then compute two deviation scores as follows:

$$D^N(\mathbf{h}^N) = 1 - c_{sim}(\mathbf{h}^N, \bar{\mathbf{h}}^N) \in [0, 2], \quad (7)$$

$$D^A(\mathbf{h}^A) = 1 - c_{sim}(\mathbf{h}^A, \bar{\mathbf{h}}^A) \in [0, 2] \quad (8)$$

These two scores are combined to produce the patch-level anomaly score as $A_{score} = D^N(\mathbf{h}^N) + D^A(\mathbf{h}^A)$.

At inference, given a normal input image, its associations with both normal and abnormal pathology terms should closely resemble those observed during training. In contrast, an abnormal image is likely to exhibit different interactions with both term pools, resulting in higher deviation scores. Consequently, abnormal images tend to produce higher anomaly scores compared to normal images.

For the WSI-level AD, splitting a WSI into a set of disjoint image patches, we compute the patch-level anomaly score A_{score} for each patch and assign the scores to their corresponding locations, thereby creating an anomaly score heatmap. Following [21], we apply 3x3 erosion operation to smooth the heatmap. Two different approaches are employed to obtain the final WSI-level anomaly score: 1) Maximum anomaly score: $A_{score}^{\max} = \max(A_{score})$ and 2) Average of the top 1% anomaly scores: $A_{score}^{\text{top1\%}} = \frac{1}{|\mathcal{K}|} \sum_{k \in \mathcal{K}} A_{score}(k)$ where \mathcal{K} represents top 1% patches.

4. Experiments and Results

Dataset. Two lymph node datasets are utilized in this study: **GastricLN** and **Camelyon16** [10]. **GastricLN** is

composed of 808 gastric lymph node WSIs (751 normal and 57 metastasis), digitized at 20x magnification, acquired from two hospitals. These WSIs are divided into training (643 normal WSIs), validation (50 normal WSIs), and test (58 normal and 57 metastasis WSIs) sets. **Camelyon16** is solely used for external testing, comprising 129 WSIs of breast lymph node, scanned at 40x magnification, (80 normal WSIs and 49 metastasis WSIs). Following [21], 22 macro-metastasis WSIs with ≥ 2 mm tumor cell diameter and 80 normal WSIs form **Camelyon16_{macro}** and are used to assess the effect of metastatic regions size on AD performance. Since most WSIs in **GastricLN** contain macro-metastases, we do not explicitly define a macro dataset for **GastricLN**. Following [18], WSIs are split into patches of size 256x256 pixels and 512x512 pixels for **GastricLN** and **Camelyon16**, respectively.

Evaluation metric. To evaluate AD performance at patch-level, we employ the area under the receiver operating characteristic curve (AUROC). For WSI-level performance, both AUROC and the area under the precision-recall curve (AUPR) are utilized. We compute the 95% confidence interval for both AUROC and AUPR by 2000-fold bootstrapping by 100% resampling with replacement.

Comparative experiments. Seven visual AD models are employed for comparison, including two student-teacher framework-based methods: STFPM [38] and EfficientAD [2], two representation-based methods: FastFlow [45] and CFA [20], two reconstruction-based methods: GANomaly [1] and AnoDDPM [42], and one VLM-based method: AnomalyCLIP [48]. The details of these methods are illustrated in the supplementary material.

Implementation detail. We use the text prompt "an image showing KEYWORD" for the text encoder of VLM Γ^T , where KEYWORD is replaced by pathology terms. The MLP consists of three linear layers with ReLU activations in the first two, mapping a 1024-dimensional input to a 128-dimensional output. For optimization, we employ the Adam optimizer with a learning rate of 0.001 and a batch size of 100. For each batch, gradients are accumulated and updated after processing 100 batches. The training process runs for a single epoch on the training set of **GastricLN** due to its large size. The normal and abnormal text-augmented centroid embeddings are obtained from the validation set of **GastricLN**. For computational reasons, AnoDDPM is evaluated on an NVIDIA RTX A6000, while the other models are evaluated on an NVIDIA RTX 3090 GPU. The specific training strategies for the seven competing models are illustrated in the supplementary material.

4.1. Main results

Tab. 1 demonstrates AD performance on two datasets using Ano-NAViLa and seven competing models. First, patch-level AD performance was assessed as the models were

trained, validated, and tested on **GastricLN**. Ano-NAViLa achieved a superior performance of 0.9681 AUROC, substantially outperforming its competitors. Next, the trained models were used to evaluate WSI-level AD performance. Ano-NAViLa attained 0.9967 and 0.9894 AUROCs and 0.9971 and 0.9904 AUPRs using A_{score}^{max} and $A_{score}^{top1\%}$, respectively. For both patch-level and WSI-level AD, STFPM was the second-best model, followed by CFA and FastFlow. These competing models fell short by 0.0097–0.0666 in AUROC and 0.0190–0.1143 in AUPR across the two anomaly scores. Finally, as the models were applied to **Camelyon16**, we observed a large performance gap between Ano-NAViLa and other models. Ano-NAViLa attained substantial gains of 0.1436–0.3778 in AUROC and 0.1447–0.4297 in AUPR for A_{score}^{max} and 0.0347–0.2689 in AUROC and 0.0903–0.3470 in AUPR for $A_{score}^{top1\%}$. The performance gains by Ano-NAViLa were even more pronounced on **Camelyon16_{macro}**, with AUROCs of 0.9858 and 0.9761, and AUPRs of 0.9547 and 0.9699 using A_{score}^{max} and $A_{score}^{top1\%}$, respectively, detecting macro-metastases almost perfectly and significantly outperforming other methods. The performance margins were even greater, such as 0.2148–0.4472 in AUROC and 0.3233–0.7288 in AUPR using A_{score}^{max} . It is worth noting that **GastricLN** and **Camelyon16** contain different organ types (i.e., gastric and breast) acquired from different institutions, likely subject to domain shifts. Nonetheless, Ano-NAViLa demonstrated superior accuracy and robustness to domain shifts across both organ types and institutions, highlighting its potential for clinical translation and application.

Tab. 2 shows the computational efficiency of Ano-NAViLa and other competing models, measured using a batch size of 28. The metrics include the number of trainable parameters (in millions, M), latency (time required for a model to process an image and generate the anomaly score, in milliseconds, ms), and peak GPU memory usage (in mebibytes, MiB). Ano-NAViLa was the most efficient model with respect to the number of trainable parameters, while it ranked second in latency and fourth in memory requirement, largely due to the usage of a VLM. Hence, optimizing the VLM could further improve the computational efficiency of Ano-NAViLa.

We visualize the WSI-level AD results as heatmaps in Fig. 3 and Fig. S1 (see supplementary material). The visualization includes Ano-NAViLa, three other models with the highest AD performance, and ground truth images, with metastatic regions highlighted in red. Due to the differences in scoring schemes and scales, we normalized the original anomaly scores using z-scores based on the mean and standard deviation of 58 normal WSIs in the test set of **GastricLN**. Ano-NAViLa clearly distinguishes normal and abnormal regions, closely matching ground truth annotations across both datasets (**GastricLN** and **Camelyon16**). Most

Method	GastricLN (WSI)				Patch	Camelyon16				Camelyon16 _{macro}			
	AUROC (A_{score}^{max})	AUPR (A_{score}^{max})	AUROC ($A_{score}^{top1\%}$)	AUPR ($A_{score}^{top1\%}$)		AUROC (A_{score}^{max})	AUPR (A_{score}^{max})	AUROC ($A_{score}^{top1\%}$)	AUPR ($A_{score}^{top1\%}$)	AUROC (A_{score}^{max})	AUPR (A_{score}^{max})	AUROC ($A_{score}^{top1\%}$)	AUPR ($A_{score}^{top1\%}$)
GANomaly	0.3947 [0.30, 0.50]	0.4323 [0.33, 0.55]	0.3125 [0.22, 0.41]	0.3958 [0.30, 0.50]	0.4182 [0.42, 0.42]	0.6503 [0.55, 0.75]	0.5519 [0.41, 0.70]	0.6643 [0.57, 0.76]	0.5445 [0.41, 0.69]	0.6631 [0.54, 0.79]	0.3873 [0.21, 0.57]	0.6494 [0.51, 0.78]	0.3575 [0.19, 0.55]
STFPM	0.9779 [0.95, 1.00]	0.9728 [0.93, 1.00]	0.9797 [0.95, 1.00]	0.9714 [0.93, 1.00]	0.9538 [0.95, 0.96]	0.7158 [0.62, 0.80]	0.6862 [0.55, 0.79]	0.7324 [0.64, 0.82]	0.7038 [0.58, 0.81]	0.7710 [0.63, 0.89]	0.6314 [0.42, 0.80]	0.7818 [0.65, 0.90]	0.6457 [0.42, 0.82]
FastFlow	0.9301 [0.87, 0.98]	0.8898 [0.78, 0.97]	0.9446 [0.89, 1.00]	0.8761 [0.76, 0.99]	0.9242 [0.92, 0.93]	0.6990 [0.61, 0.79]	0.6304 [0.50, 0.75]	0.7337 [0.64, 0.82]	0.6335 [0.48, 0.78]	0.7239 [0.59, 0.85]	0.5291 [0.31, 0.71]	0.7705 [0.64, 0.88]	0.4976 [0.30, 0.75]
CFA	0.9673 [0.93, 1.00]	0.9243 [0.82, 1.00]	0.9570 [0.90, 1.00]	0.8876 [0.77, 1.00]	0.8881 [0.89, 0.89]	0.7003 [0.60, 0.79]	0.6435 [0.50, 0.76]	0.7355 [0.64, 0.83]	0.6718 [0.53, 0.80]	0.7574 [0.61, 0.88]	0.6008 [0.37, 0.79]	0.7699 [0.63, 0.90]	0.5557 [0.34, 0.78]
AnoDDPM	0.8860 [0.82, 0.94]	0.8739 [0.78, 0.94]	0.8621 [0.79, 0.93]	0.8403 [0.73, 0.93]	0.8860 [0.88, 0.89]	0.4816 [0.37, 0.63]	0.4012 [0.15, 0.40]	0.5013 [0.34, 0.64]	0.4471 [0.17, 0.49]	0.5386 [0.42, 0.66]	0.2259 [0.15, 0.36]	0.6631 [0.54, 0.78]	0.4353 [0.25, 0.62]
EfficientAD	0.8772 [0.79, 0.95]	0.7856 [0.65, 0.91]	0.8817 [0.80, 0.95]	0.7539 [0.62, 0.91]	0.8432 [0.84, 0.85]	0.6462 [0.55, 0.74]	0.5170 [0.38, 0.66]	0.6526 [0.55, 0.75]	0.5364 [0.40, 0.69]	0.6415 [0.51, 0.77]	0.3067 [0.17, 0.51]	0.6006 [0.45, 0.74]	0.2928 [0.16, 0.48]
AnomalyCLIP	0.7371 [0.64, 0.82]	0.7057 [0.58, 0.83]	0.5309 [0.43, 0.64]	0.5054 [0.40, 0.65]	0.3314 [0.33, 0.33]	0.6003 [0.50, 0.69]	0.4830 [0.35, 0.62]	0.5446 [0.44, 0.65]	0.4568 [0.33, 0.58]	0.6187 [0.48, 0.75]	0.3480 [0.18, 0.54]	0.5392 [0.39, 0.69]	0.3402 [0.17, 0.52]
Ano-NAViLa	0.9967 [0.99, 1.00]	0.9971 [0.99, 1.00]	0.9894 [0.97, 1.00]	0.9904 [0.98, 1.00]	0.9681 [0.97, 0.97]	0.8594 [0.79, 0.92]	0.8309 [0.73, 0.91]	0.7702 [0.67, 0.86]	0.7941 [0.69, 0.88]	0.9858 [0.96, 1.00]	0.9547 [0.88, 1.00]	0.9761 [0.92, 1.00]	0.9699 [0.89, 1.00]

Table 1. AD performance on GastricLN and Camelyon16 datasets.

Method	Params [M]	Latency [ms]	GPU [MiB]	Method	GastricLN (WSI)				Patch	Camelyon16			
					AUROC (A_{score}^{max})	AUPR (A_{score}^{max})	AUROC ($A_{score}^{top1\%}$)	AUPR ($A_{score}^{top1\%}$)		AUROC (A_{score}^{max})	AUPR (A_{score}^{max})	AUROC ($A_{score}^{top1\%}$)	AUPR ($A_{score}^{top1\%}$)
GANomaly	188.69	1.45	1580	Sum	0.9967 [0.99, 1.00]	0.9971 [0.99, 1.00]	0.9894 [0.97, 1.00]	0.9904 [0.98, 1.00]	0.9681 [0.97, 0.97]	0.8594 [0.79, 0.93]	0.8309 [0.73, 0.91]	0.7702 [0.67, 0.86]	0.7941 [0.69, 0.88]
STFPM	2.78	14.76	504	Max	0.9967 [0.99, 1.00]	0.9971 [0.99, 1.00]	0.9888 [0.97, 1.00]	0.9899 [0.97, 1.00]	0.9669 [0.97, 0.97]	0.8566 [0.78, 0.92]	0.8197 [0.71, 0.90]	0.7719 [0.68, 0.86]	0.7854 [0.68, 0.87]
FastFlow	45.01	26.21	1700	L2-norm	0.9967 [0.99, 1.00]	0.9971 [0.99, 1.00]	0.9888 [0.97, 1.00]	0.9899 [0.97, 1.00]	0.9678 [0.97, 0.97]	0.8592 [0.79, 0.92]	0.8258 [0.72, 0.90]	0.7712 [0.68, 0.86]	0.7880 [0.68, 0.87]
CFA	31.29	8.58	10990	AE	0.9967 [0.99, 1.00]	0.9971 [0.99, 1.00]	0.9909 [0.98, 1.00]	0.9921 [0.98, 1.00]	0.9575 [0.96, 0.96]	0.8597 [0.79, 0.92]	0.8270 [0.73, 0.90]	0.7934 [0.70, 0.88]	0.8013 [0.70, 0.88]
AnoDDPM	113.67	915.56	10712	SVM-r	0.9967 [0.99, 1.00]	0.9971 [0.99, 1.00]	0.9794 [0.95, 1.00]	0.9846 [0.96, 1.00]	0.9464 [0.95, 0.95]	0.8005 [0.71, 0.87]	0.7473 [0.62, 0.86]	0.7457 [0.64, 0.84]	0.7739 [0.67, 0.86]
EfficientAD	8.06	3.86	2774	SVM-a	0.9967 [0.99, 1.00]	0.9971 [0.99, 1.00]	0.9782 [0.94, 1.00]	0.9837 [0.96, 1.00]	0.9456 [0.95, 0.95]	0.8135 [0.73, 0.88]	0.7857 [0.67, 0.87]	0.7454 [0.64, 0.84]	0.7716 [0.67, 0.86]
AnomalyCLIP	5.56	16.86	3176	GMM-r	0.9970 [0.99, 1.00]	0.9974 [0.99, 1.00]	0.9915 [0.98, 1.00]	0.9923 [0.98, 1.00]	0.9566 [0.96, 0.96]	0.8577 [0.79, 0.92]	0.8071 [0.70, 0.90]	0.7941 [0.70, 0.88]	0.8013 [0.71, 0.88]
Ano-NAViLa	0.69	3.61	2098	GMM-a	0.9964 [0.99, 1.00]	0.9969 [0.99, 1.00]	0.9909 [0.98, 1.00]	0.9919 [0.98, 1.00]	0.9563 [0.96, 0.96]	0.8582 [0.79, 0.92]	0.8073 [0.69, 0.90]	0.7959 [0.71, 0.88]	0.8011 [0.70, 0.88]

Table 2. Computational efficiency.

Table 3. AD performance with different anomaly scoring methods.

of metastatic regions are highlighted with higher anomaly scores, facilitating precise localization of metastatic regions in WSIs. However, other models struggled to detect metastatic regions, producing either less confident or overly specific heatmaps. For example, in the second row of Fig. 3, though these models assign slightly higher scores to the metastatic regions than to normal regions, the distinction between the two regions was not as clear as in Ano-NAViLa, posing a risk of missing the metastatic regions. In the sixth row of Fig. 3, these models primarily highlight only the boundaries of metastatic regions, i.e., missing majority of metastatic regions, while also highlighting the boundaries of normal tissues, leading to false positives. These observations further strengthen the superior ability of Ano-NAViLa, particularly on **Camelyon16**.

4.2. Ablation study

We conduct ablation studies from two perspectives: 1) Composition of text-augmented image embeddings; 2) Generation of anomaly scores.

Composition of text-augmented image embeddings.

To analyze the effect of text-augmented image embeddings on AD performance, we conducted experiments using four

different combinations of the image embedding \mathbf{v}^I and two text embeddings \mathbf{v}^N and \mathbf{v}^A : 1) text embeddings only: \mathbf{v}^N and \mathbf{v}^A ; 2) image embedding only: \mathbf{v}^I ; 3) image embedding and normal text embedding: \mathbf{v}^I and \mathbf{v}^N ; 4) image embedding and both text embeddings: \mathbf{v}^I , \mathbf{v}^N , and \mathbf{v}^A (Ours). Tab. 4 presents the results of these four experiments. The absence of any of the three embeddings resulted in a performance drop in all cases, except for AUROC using \mathbf{v}^I and $A_{score}^{top1\%}$ on **Camelyon16**. Among the three embeddings, the image embedding \mathbf{v}^I had the greatest impact on AD performance, as using text embeddings only resulted in the largest performance drop. While the addition of the normal text embedding \mathbf{v}^N to the image embedding \mathbf{v}^I was not beneficial on **GastricLN**, the addition boosted AD performance on **Camelyon16**. Furthermore, adding the abnormal text embedding \mathbf{v}^A improved AD performance for both datasets. These findings suggest a synergistic effect between normal and abnormal text embeddings. Notably, using text embeddings only, we obtained comparable performance to STFPM, which is the top-performing model among other competitors.

Moreover, to ensure that the performance gain does not merely originate from the use of the VLM backbone, we

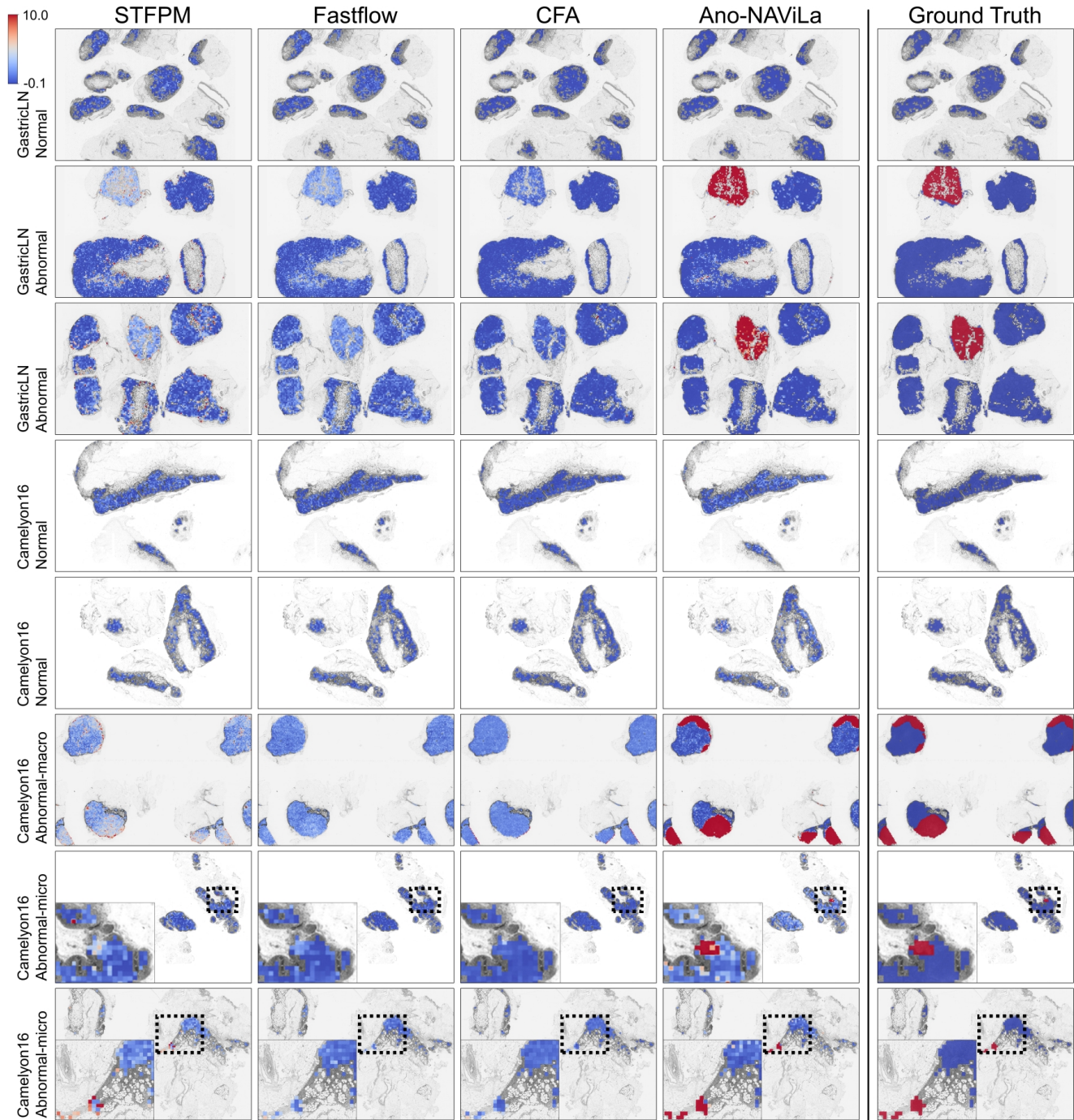


Figure 3. Visualization of anomaly localization in WSIs.

evaluated the zero-shot performance of CONCH using the same term pools. As shown in Table S2 (see supplementary material), the results are significantly lower than Ano-NAViLa, demonstrating that the proposed framework contributes substantially beyond the capabilities of the VLM.

Generation of anomaly scores. To compute the patch-level anomaly score A_{score} , we simply sum the two devi-

ation scores D^N and D^A . To assess its effectiveness, we compared it with five other approaches, including two simple approaches, such as maximum and L2-norm of the two deviation scores, and three methods requiring additional training, namely autoencoder (AE), one-class SVM (SVM), and Gaussian mixture model (GMM). AE is trained using the entire training set of **GastricLN**, while SVM and GMM

Embeddings	GastricLN (WSI)				Patch	Camelyon16				Camelyon16 _{macro}			
	AUROC (A_{score}^{max})	AUPR (A_{score}^{max})	AUROC ($A_{score}^{top1\%}$)	AUPR ($A_{score}^{top1\%}$)	AUROC	AUROC (A_{score}^{max})	AUPR (A_{score}^{max})	AUROC ($A_{score}^{top1\%}$)	AUPR ($A_{score}^{top1\%}$)	AUROC (A_{score}^{max})	AUPR (A_{score}^{max})	AUROC ($A_{score}^{top1\%}$)	AUPR ($A_{score}^{top1\%}$)
v^N, v^A	0.9749 [0.94, 1.00]	0.9748 [0.94, 1.00]	0.9685 [0.94, 1.00]	0.9717 [0.94, 1.00]	0.8309 [0.83, 0.83]	0.7292 [0.63, 0.82]	0.6164 [0.48, 0.76]	0.7411 [0.65, 0.83]	0.7085 [0.58, 0.81]	0.7855 [0.66, 0.90]	0.5705 [0.35, 0.78]	0.8903 [0.79, 0.97]	0.7968 [0.62, 0.92]
v^I	0.9902 [0.97, 1.00]	0.9922 [0.98, 1.00]	0.9828 [0.96, 1.00]	0.9844 [0.96, 1.00]	0.9651 [0.96, 0.97]	0.7857 [0.70, 0.86]	0.6844 [0.54, 0.80]	0.7898 [0.70, 0.87]	0.7569 [0.63, 0.86]	0.8940 [0.83, 0.95]	0.6931 [0.48, 0.85]	0.9557 [0.89, 0.99]	0.8847 [0.73, 0.98]
v^I, v^N	0.9799 [0.96, 1.00]	0.9806 [0.96, 1.00]	0.9704 [0.94, 1.00]	0.9698 [0.94, 1.00]	0.9515 [0.95, 0.95]	0.7980 [0.71, 0.88]	0.7187 [0.58, 0.84]	0.7667 [0.68, 0.85]	0.7667 [0.66, 0.86]	0.9043 [0.83, 0.96]	0.7196 [0.51, 0.88]	0.9636 [0.92, 1.00]	0.9222 [0.82, 0.99]
v^I, v^N, v^A (Ours)	0.9967 [0.99, 1.00]	0.9971 [0.99, 1.00]	0.9894 [0.97, 1.00]	0.9904 [0.98, 1.00]	0.9681 [0.97, 0.97]	0.8594 [0.79, 0.92]	0.8309 [0.73, 0.91]	0.7702 [0.67, 0.86]	0.7941 [0.69, 0.88]	0.9858 [0.96, 1.00]	0.9547 [0.88, 1.00]	0.9761 [0.92, 1.00]	0.9699 [0.89, 1.00]

Table 4. Results of ablation study.

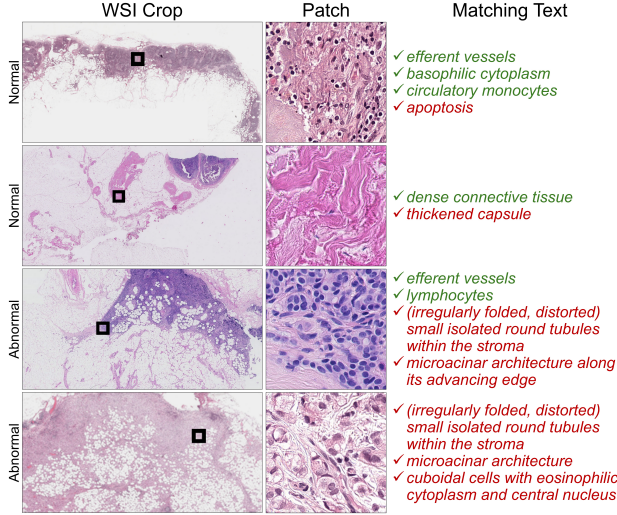


Figure 4. Exemplary WSIs from Camelyon16 and their matching pathology terms. Normal and abnormal terms are shown in green and red, respectively.

are trained using two approaches: 1) using a random subset of the training set, resulting in SVM-r and GMM-r; 2) applying AdaBoost[11] with 10 iterations, resulting in SVM-a and GMM-a. As shown in Tab. 3, AD performance was not substantially dependent on a specific scoring scheme. Although there was a favorable method for each task/dataset, the difference was minimal. These findings further emphasize the strength of the text-augmented image embeddings.

Furthermore, we repeated the entire experiments without the erosion operation for heatmap smoothing. The experimental results, provided in the supplementary material, show that Ano-NAViLa’s performance remained consistent, regardless of the erosion operation. In contrast, other competing models were generally sensitive to its use. These observations further confirm the robustness of Ano-NAViLa.

4.3. Visual and textual association and explanation

We examined each WSI and its matching pathology terms to verify the accuracy and relevance of the image-text association through the VLM. Fig. 4 presents exemplary Camelyon16 WSIs, representative patches with the highest

anomaly scores, and top-matching pathology terms identified by Ano-NAViLa. These selected pathology terms were reviewed and validated by an experienced pathologist. We found that the selected patches are not only representative of the WSI class label, but also that the matching pathology terms are highly relevant to both the patches and their respective class labels. These suggest that Ano-NAViLa effectively identifies relevant patches, infers disease status based on these patches, and produces histologically meaningful textual descriptions.

Moreover, we compared the distribution of image-text similarities in both GastricLN and Camelyon16 as shown in Fig. S2 and S3 (see supplementary material). Despite differences between two datasets, the image-text similarity distributions remained consistent for patches with the same label. Specifically, in the normal term pool, certain terms (e.g., 1. *Helper T lymphocyte*, 2. *Small dormant lymphocytes*) exhibited higher similarity with normal-labeled patches for both datasets. Abnormal-labeled patches displayed a different distribution of similarity scores to normal patches. Similar trends were found at the WSI-level. Within the abnormal term pool, 1. *Tumor buds that emerge from medium-sized tubules* consistently showed high similarity exclusively at both patch- and WSI-levels across the two datasets. These results further support the consistent performance of Ano-NAViLa.

5. Conclusions

We present Ano-NAViLa, a model that detects anomalous pathology images by utilizing expert knowledge of normal and abnormal histopathology as well as data-driven knowledge from a pre-trained VLM trained on a vast amount of pathology image-text data. The experimental results demonstrate that Ano-NAViLa not only surpasses existing AD methods in performance but also enhances interpretability through pathology image-text associations, holding great potential for clinical translation and application. Future study will entail developing an automated protocol to construct pathology term pools for broader applications, extending validation with external datasets across various organs, and optimizing the model, particularly the VLM, to enhance computational efficiency.

Acknowledgments This work was supported by a grant of the National Research Foundation of Korea (NRF), South Korea (No. RS-2024-00397293 and RS-2025-00558322) and Korea Institute for Advancement of Technology (KIAT) through the International Cooperative R&D program (No. P0022543). GastricLN dataset was collected from Korea University Anam Hospital and The Catholic University of Korea, Seoul St. Mary's Hospital.

References

- [1] Samet Akcay, Amir Atapour-Abarghouei, and Toby P. Breckon. Ganomaly: Semi-supervised anomaly detection via adversarial training. In *Computer Vision – ACCV 2018*, pages 622–637, 2019. 2, 5
- [2] Kilian Batzner, Lars Heckler, and Rebecca König. Efficientad: Accurate visual anomaly detection at millisecond-level latencies. In *Proceedings of the IEEE/CVF Winter Conference on Applications of Computer Vision*, pages 128–138, 2024. 2, 5
- [3] Christoph Baur, Benedikt Wiestler, Shadi Albarqouni, and Nassir Navab. Deep autoencoding models for unsupervised anomaly segmentation in brain mr images. In *Brainlesion: Glioma, Multiple Sclerosis, Stroke and Traumatic Brain Injuries*, pages 161–169, 2019. 2
- [4] Paul Bergmann, Michael Fauser, David Sattlegger, and Carsten Steger. Mvtec ad — a comprehensive real-world dataset for unsupervised anomaly detection. In *Proceedings of the IEEE/CVF Conference on Computer Vision and Pattern Recognition (CVPR)*, pages 9584–9592, 2019. 1
- [5] Paul Bergmann, Michael Fauser, David Sattlegger, and Carsten Steger. Uninformed students: Student-teacher anomaly detection with discriminative latent embeddings. In *Proceedings of the IEEE/CVF conference on computer vision and pattern recognition*, pages 4183–4192, 2020. 2
- [6] Corinna Cortes and Vladimir Vapnik. Support-vector networks. *Machine Learning*, 20(3):273–297, 1995. 2
- [7] Thomas Defard, Aleksandr Setkov, Angelique Loesch, and Romaric Audigier. Padim: a patch distribution modeling framework for anomaly detection and localization. In *International Conference on Pattern Recognition*, pages 475–489. Springer, 2021. 1, 2
- [8] Hanqiu Deng and Xingyu Li. Anomaly detection via reverse distillation from one-class embedding. In *Proceedings of the IEEE/CVF conference on computer vision and pattern recognition*, pages 9737–9746, 2022. 1
- [9] Jonas Dippel, Niklas Prenil, Julius Hense, Philipp Liznerski, Tobias Winterhoff, Simon Schallenberg, Marius Kloft, Oliver Buchstab, David Horst, Maximilian Alber, et al. Ai-based anomaly detection for clinical-grade histopathological diagnostics. *NEJM AI*, 1(11):AIoa2400468, 2024. 1
- [10] Babak Ehteshami Bejnordi, Mitko Veta, Paul Johannes van Diest, Bram van Ginneken, Nico Karssemeijer, Geert Litjens, Jeroen A. W. M. van der Laak, and the CAMELYON16 Consortium. Diagnostic assessment of deep learning algorithms for detection of lymph node metastases in women with breast cancer. *JAMA*, 318(22):2199–2210, 2017. 2, 4
- [11] Yoav Freund, Robert E Schapire, et al. Experiments with a new boosting algorithm. In *icml*, pages 148–156. Citeseer, 1996. 8
- [12] Neal S. Goldstein and John Hart. Histologic features associated with lymph node metastasis in stage t1 and superficial t2 rectal adenocarcinomas in abdominoperineal resection specimens: Identifying a subset of patients for whom treatment with adjuvant therapy or completion abdominoperineal resection should be considered after local excision. *American Journal of Clinical Pathology*, 111(1):51–58, 1999. 3
- [13] Denis Gudovskiy, Shun Ishizaka, and Kazuki Kozuka. Cflow-ad: Real-time unsupervised anomaly detection with localization via conditional normalizing flows. In *Proceedings of the IEEE/CVF winter conference on applications of computer vision*, pages 98–107, 2022. 1, 2
- [14] Zhi Huang, Federico Bianchi, Mert Yuksekgonul, Thomas J Montine, and James Zou. A visual–language foundation model for pathology image analysis using medical twitter. *Nature medicine*, 29(9):2307–2316, 2023. 2
- [15] Wisdom Ikezogwo, Saygin Seyfioglu, Fatemeh Ghezloo, Dylan Geva, Fatwir Sheikh Mohammed, Pavan Kumar Anand, Ranjay Krishna, and Linda Shapiro. Quilt-1m: One million image-text pairs for histopathology. *Advances in neural information processing systems*, 36, 2024. 2
- [16] Jongheon Jeong, Yang Zou, Taewan Kim, Dongqing Zhang, Avinash Ravichandran, and Onkar Dabeer. Winclip: Zero/few-shot anomaly classification and segmentation. In *Proceedings of the IEEE/CVF Conference on Computer Vision and Pattern Recognition*, pages 19606–19616, 2023. 2
- [17] Chao Jia, Yinfei Yang, Ye Xia, Yi-Ting Chen, Zarana Parekh, Hieu Pham, Quoc Le, Yun-Hsuan Sung, Zhen Li, and Tom Duerig. Scaling up visual and vision-language representation learning with noisy text supervision. In *International conference on machine learning*, pages 4904–4916. PMLR, 2021. 2
- [18] Jun Jiang, Burak Tekin, Lin Yuan, Sebastian Armasu, Stacey J Winham, Ellen L Goode, Hongfang Liu, Yajue Huang, Ruifeng Guo, and Chen Wang. Computational tumor stroma reaction evaluation led to novel prognosis-associated fibrosis and molecular signature discoveries in high-grade serous ovarian carcinoma. *Frontiers in Medicine*, 9:994467, 2022. 5
- [19] Daisuke Komura and Shumpei Ishikawa. Machine learning methods for histopathological image analysis. *Computational and structural biotechnology journal*, 16:34–42, 2018. 1
- [20] Sungwook Lee, Seunghyun Lee, and Byung Cheol Song. Cfa: Coupled-hypersphere-based feature adaptation for target-oriented anomaly localization. *IEEE Access*, 10: 78446–78454, 2022. 2, 5
- [21] Jasper Linmans, Gabriel Raya, Jeroen van der Laak, and Geert Litjens. Diffusion models for out-of-distribution detection in digital pathology. *Medical Image Analysis*, 93: 103088, 2024. 1, 2, 4, 5
- [22] Wenqian Liu, Runze Li, Meng Zheng, Srikrishna Karanam, Ziyang Wu, Bir Bhanu, Richard J. Radke, and Octavia Camps.

- Towards visually explaining variational autoencoders. In *2020 IEEE/CVF Conference on Computer Vision and Pattern Recognition (CVPR)*, pages 8639–8648, Los Alamitos, CA, USA, 2020. IEEE Computer Society. 2
- [23] Philipp Liznerski, Lukas Ruff, Robert A. Vandermeulen, Billy Joe Franks, Marius Kloft, and Klaus-Robert Müller. Explainable deep one-class classification. In *International Conference on Learning Representations*, 2021. 2
- [24] Ming Y Lu, Bowen Chen, Drew FK Williamson, Richard J Chen, Ivy Liang, Tong Ding, Guillaume Jaume, Igor Odintsov, Long Phi Le, Georg Gerber, et al. A visual-language foundation model for computational pathology. *Nature Medicine*, 30:863–874, 2024. 2, 4
- [25] Phuc Cuong Ngo, Amadeus Aristo Winarto, Connie Khor Li Kou, Sojeong Park, Farhan Akram, and Hwee Kuan Lee. Fence gan: Towards better anomaly detection. In *2019 IEEE 31st International Conference on Tools with Artificial Intelligence (ICTAI)*, pages 141–148, 2019. 2
- [26] Anh Tien Nguyen, Trinh Thi Le Vuong, and Jin Tae Kwak. Towards a text-based quantitative and explainable histopathology image analysis. In *International Conference on Medical Image Computing and Computer-Assisted Intervention*, pages 514–524. Springer, 2024. 3
- [27] Taesung Park, Ming-Yu Liu, Ting-Chun Wang, and Jun-Yan Zhu. Semantic image synthesis with spatially-adaptive normalization. In *Proceedings of the IEEE/CVF Conference on Computer Vision and Pattern Recognition (CVPR)*, 2019. 2
- [28] Alec Radford, Jong Wook Kim, Chris Hallacy, Aditya Ramesh, Gabriel Goh, Sandhini Agarwal, Girish Sastry, Amanda Askell, Pamela Mishkin, Jack Clark, et al. Learning transferable visual models from natural language supervision. In *International conference on machine learning*, pages 8748–8763. PMLR, 2021. 2
- [29] Oliver Rippel, Patrick Mertens, Eike König, and Dorit Merhof. Gaussian anomaly detection by modeling the distribution of normal data in pretrained deep features. *IEEE Transactions on Instrumentation and Measurement*, 70:1–13, 2021. 2
- [30] Oliver Rippel, Patrick Mertens, and Dorit Merhof. Modeling the distribution of normal data in pre-trained deep features for anomaly detection. In *2020 25th International Conference on Pattern Recognition (ICPR)*, pages 6726–6733. IEEE, 2021. 2
- [31] Karsten Roth, Latha Pemula, Joaquin Zepeda, Bernhard Schölkopf, Thomas Brox, and Peter Gehler. Towards total recall in industrial anomaly detection. In *Proceedings of the IEEE/CVF conference on computer vision and pattern recognition*, pages 14318–14328, 2022. 1
- [32] Karsten Roth, Latha Pemula, Joaquin Zepeda, Bernhard Schölkopf, Thomas Brox, and Peter Gehler. Towards total recall in industrial anomaly detection. In *Proceedings of the IEEE/CVF Conference on Computer Vision and Pattern Recognition (CVPR)*, pages 14318–14328, 2022. 1, 2
- [33] Marco Rudolph, Tom Wehrbein, Bodo Rosenhahn, and Bastian Wandt. Fully convolutional cross-scale-flows for image-based defect detection. In *Proceedings of the IEEE/CVF Winter Conference on Applications of Computer Vision*, pages 1088–1097, 2022. 2
- [34] Marco Rudolph, Tom Wehrbein, Bodo Rosenhahn, and Bastian Wandt. Asymmetric student-teacher networks for industrial anomaly detection. In *Proceedings of the IEEE/CVF winter conference on applications of computer vision*, pages 2592–2602, 2023. 1, 2
- [35] Mohammadreza Salehi, Niousha Sadjadi, Soroosh Baselizadeh, Mohammad H Rohban, and Hamid R Rabiee. Multiresolution knowledge distillation for anomaly detection. In *Proceedings of the IEEE/CVF conference on computer vision and pattern recognition*, pages 14902–14912, 2021. 2
- [36] Thomas Schlegl, Philipp Seeböck, Sebastian M. Waldstein, Ursula Schmidt-Erfurth, and Georg Langs. Unsupervised anomaly detection with generative adversarial networks to guide marker discovery. In *Information Processing in Medical Imaging*, pages 146–157, 2017. 2
- [37] Jiayu Sun, Xinzhou Wang, Naixue Xiong, and Jie Shao. Learning sparse representation with variational auto-encoder for anomaly detection. *IEEE Access*, 6:33353–33361, 2018. 2
- [38] Guodong Wang, Shumin Han, Errui Ding, and Di Huang. Student-teacher feature pyramid matching for anomaly detection. *The British Machine Vision Conference (BMVC)*, 2021. 2, 5
- [39] Zirui Wang, Jiahui Yu, Adams Wei Yu, Zihang Dai, Yulia Tsvetkov, and Yuan Cao. Simvlm: Simple visual language model pretraining with weak supervision. In *International Conference on Learning Representations*, 2022. 2
- [40] Svante Wold, Kim Esbensen, and Paul Geladi. Principal component analysis. *Chemometrics and Intelligent Laboratory Systems*, 2(1):37–52, 1987. Proceedings of the Multivariate Statistical Workshop for Geologists and Geochemists. 2
- [41] Jihui-Ciang Wu, Ding-Jie Chen, Chiou-Shann Fuh, and Tyng-Luh Liu. Learning unsupervised metaformer for anomaly detection. In *Proceedings of the IEEE/CVF International Conference on Computer Vision (ICCV)*, pages 4369–4378, 2021. 2
- [42] Julian Wyatt, Adam Leach, Sebastian M. Schmon, and Chris G. Willcocks. Anoddpn: Anomaly detection with denoising diffusion probabilistic models using simplex noise. In *Proceedings of the IEEE/CVF Conference on Computer Vision and Pattern Recognition (CVPR) Workshops*, pages 650–656, 2022. 1, 2, 5
- [43] Cheng Yan, Shiyu Zhang, Yang Liu, Guansong Pang, and Wenjun Wang. Feature prediction diffusion model for video anomaly detection. In *Proceedings of the IEEE/CVF International Conference on Computer Vision (ICCV)*, pages 5527–5537, 2023. 2
- [44] Jihun Yi and Sungroh Yoon. Patch svdd: Patch-level svdd for anomaly detection and segmentation. In *Proceedings of the Asian conference on computer vision*, 2020. 2
- [45] Jiawei Yu, Ye Zheng, Xiang Wang, Wei Li, Yushuang Wu, Rui Zhao, and Liwei Wu. Fastflow: Unsupervised anomaly detection and localization via 2d normalizing flows. *arXiv preprint arXiv:2111.07677*, 2021. 1, 2, 5
- [46] Jiahui Yu, Zirui Wang, Vijay Vasudevan, Legg Yeung, Mojtaba Seyedhosseini, and Yonghui Wu. Coca: Contrastive

captioners are image-text foundation models. *Transactions on Machine Learning Research*, 2022. [2](#)

- [47] Sheng Zhang, Yanbo Xu, Naoto Usuyama, Hanwen Xu, Jaspreet Bagga, Robert Tinn, Sam Preston, Rajesh Rao, Mu Wei, Naveen Valluri, Cliff Wong, Andrea Tupini, Yu Wang, Matt Mazzola, Swadheen Shukla, Lars Liden, Jianfeng Gao, Angela Crabtree, Brian Piening, Carlo Bifulco, Matthew P. Lungren, Tristan Naumann, Sheng Wang, and Hoifung Poon. A multimodal biomedical foundation model trained from fifteen million image-text pairs. *NEJM AI*, 2(1):AIoa2400640, 2025. [2](#)
- [48] Qihang Zhou, Guansong Pang, Yu Tian, Shibo He, and Jiming Chen. Anomalyclip: Object-agnostic prompt learning for zero-shot anomaly detection. In *The Twelfth International Conference on Learning Representations*, 2023. [2](#), [5](#)
- [49] Jiawen Zhu and Guansong Pang. Toward generalist anomaly detection via in-context residual learning with few-shot sample prompts. In *Proceedings of the IEEE/CVF conference on computer vision and pattern recognition*, pages 17826–17836, 2024. [2](#)
- [50] Igor Zingman, Birgit Stierstorfer, Charlotte Lempp, and Fabian Heinemann. Learning image representations for anomaly detection: application to discovery of histological alterations in drug development. *Medical Image Analysis*, 92:103067, 2024. [1](#)
- [51] Beiji Zou, Kangkang Yang, Xiaoyan Kui, Jun Liu, Shenghui Liao, and Wei Zhao. Anomaly detection for streaming data based on grid-clustering and gaussian distribution. *Information Sciences*, 638:118989, 2023. [2](#)